Analytical Calculation of the RMS Value and the Spectrum of the DC-Link Current of a Dual-Inverter

Maximilian Schiedermeier, Franziska Schlamp, Cornelius Rettner, and Martin März

***Abstract*—This article is focused on the analytic definition of the dc-link current of a dual-inverter. Therefore, a two-level dual-inverter for driving two independent three-phase electrical motors is considered. Space-vector modulation is taken into account as the modulation method of the inverter. Based on that, an analytic description is derived for the frequency spectrum as well as for the rms value of the dc-link current of a dual-inverter. Contrary to the current definitions known from previous publications, the expressions presented below are defined in solved form. Therefore, the use of integral or differential equation expressions is not necessary. In this way, a basis is created for calculating the dc-link current without computationally intensive numerical integration processes or SPICE simulations. Furthermore, this article includes the metrological verification of the novel expressions. The results discussed in this publication provide the basis for stabilizing the HV-dc system and for minimizing the dc-link capacitor load. Thus, they enable the dc-link capacitor of a dual-inverter to be downsized. Based on the presented definition of the dc-link current in solved form, the possibility of real-time optimization is created. Furthermore, the results outlined in this article form the foundation to derive the control optimization for a multiphase inverter.**

***Index Terms*—DC-link current, dual inverter, Newton-cotes, phase shift, voltage source inverter (VSI).**

NOMENCLATURE

$A(y)$	Original function to be integrated.
$B(y)$	Approximated function which is similar to $A(y)$.
c_k	Auxiliary variable to calculate location of sampling point.
d_k	Location of sampling points.
f_{f1}, f_{f2}	Frequency of Inverter1's and Inverter2's phase currents.
$f_{\mathrm{sw1}}, f_{\mathrm{sw2}}$	Switching frequency.
g	Index of switching wave harmonic of Inverter2.
h	Index of fundamental frequency harmonic of Inverter2.
I_C	Capacitor current.
$\hat{I}_{\mathrm{calc}}(f), \hat{I}_{\mathrm{sim}}(f)$	Calculated and simulated amplitude of a harmonic of I_{Inv}.
I_{DC}	DC-current.
$I_{Inv}, I_{Inv1}, I_{Inv2}$	DC-link current of dual-inverter, Inverter1 and Inverter2.
$I_R, I_S, I_T,\ \hat{I}_{RST}$	Phase currents of Inverter2 and their amplitude.
$i_R, i_S i_T$	Time function of Inverter2's phase current.
I_R^*, I_S^*, I_T^*	Current of Inverter2's upper switches.
$I_R^{\sim}(f), I_S^{\sim}(f), I_T^{\sim}(f)$	Quasi-spectra of switch currents which result from integrating over 120°.
$I_U, I_V, I_W,\ \hat{I}_{UVW}$	Phase current of Inverter1 and their amplitude.
i_U, i_V, i_W	Time function of Inverter1's phase current.
I_U^*, I_V^*, I_W^*	Current of Inverter1's upper switches.
$I_U^{\sim}(f), I_V^{\sim}(f), I_W^{\sim}(f)$	Quasi-spectra of switch currents which result from integrating over 120°.
M_1, M_2	Modulation index with reference to phase-neural-point voltage.
$M_{\mathrm{PhPh1}}, M_{\mathrm{PhPh2}}$	Modulation index with reference to phase-phase voltage.
m	Index of switching wave harmonic of Inverter1.
n	Index of fundamental frequency harmonic of Inverter1.
T_{ic}	Period of the capacitor current time function $i_C(t)$.
$T_{\mathrm{sw1}}, T_{\mathrm{sw2}}$	Switching period time.
w_k	Newton-Cotes' weights.
x	Substituted product of time and switching angular frequency.
x_r, x_f	Inner integration limits of double Fourier integral.
y	Substituted product of time and fundamental angular frequency.
y_s, y_e	Outer integration limits of double Fourier integral.
β	Shift of Inverter1's voltage harmonic to Inverter2's voltage harmonic.
γ_1, γ_7	Continuous ON-time of S_1 and S_7 normalized on T_{sw1} and T_{sw2}.
ρ	Distribution factor of zero-vectors per switching period.

Manuscript received January 1, 2021; revised March 23, 2021 and May 14, 2021; accepted June 24, 2021. Date of publication July 8, 2021; date of current version September 16, 2021. Recommended for publication by Associate Editor D. O. Neacsu. (*Corresponding author: Maximilian Schiedermeier.*)

Maximilian Schiedermeier, Cornelius Rettner, and Martin März are with the Department of Power Electronics LEE, Friedrich-Alexander-University Erlangen-Nuremberg, 90429 Erlangen, Germany (e-mail: maximilian.schiedermeier@audi.de; cornelius.rettner@fau.de; martin.maerz@fau.de).

Franziska Schlamp is with the Faculty of Mathematics and Geography, Catholic University of Eichstätt-Ingolstadt, 85072 Eichstätt, Germany (e-mail: franziska.schlamp@ku.de).

Color versions of one or more figures in this article are available at https://doi.org/10.1109/TPEL.2021.3095520.

Digital Object Identifier 10.1109/TPEL.2021.3095520

σ	Shift of Inverter1's switch signals to Inverter2's switch signals.
φ_1, φ_2	Phase-shift of Inverter1's and Inverter2's voltage harmonics to their phase currents.
ω_{f1}, ω_{f2}	Angular frequency of Inverter1's and Inverter2's phase currents.
$\omega_{\mathrm{sw1}}, \omega_{\mathrm{sw2}}$	Switching frequency of Inverter1 and Inverter2.

I. Introduction

THE Need of regulating the flow of energy between two or more electrical motors or comparable ac-impedances and a dc-grid is given in many applications. Thereby, the use of a dual-inverter instead of two individual inverters often makes sense due to many reasons. An example of such an application can be found in the field of electrified vehicles. As explained in [1], [2], drive concepts of hybrid electric vehicles (HEVs), battery electric vehicles (BEVs), and fuel cell electric vehicles (FCEVs) are often operated with at least two electric motors. This can be explained by the advantages of performance scalability, the potential of cost savings, driving dynamics advantages (four-wheel drive, torque vectoring), and the increase in efficiency in partial load operation. The use of dual-inverters is common practice here. As one of the most expensive, heaviest, and most voluminous components of the traction inverter, the dc-link capacitor is an essential component. In the following explanations, the reduction of the capacitor load of a two-level dual-inverter for the control of two independent electrical machines, as defined in [3] and [4], is investigated. This reduction forms the basis for an optimized design of the component. The definitions and relationships discussed in this article are based on the application of the electric vehicle. However, they can be considered valid for all conceivable industrial applications, which use a dual-inverter or multiphase-inverter with two or more independent three-phase electrical motors. The RMS value of the dc-link current is described in this article not only for a single-inverter as in [5] and [6], but also for a dual-inverter. In contrast to [7], the frequency spectrum of the current is not described for a single- but for a dual-inverter. In addition to the explanations in [4], [8]–[11], the description of the spectrum is presented in a solved form. Therefore, a numerical integration for determining the dc-link current for any operating point of the dual-inverter becomes obsolete. All parameters that determine the operating point of the two electrical motors are taken into account as variables. Furthermore, the switching cycle shift of the two inverters is considered to be variable in the description of the dc-link current. As shown in [4], [8]–[10], [12], and [13], this shift in the control signals and the resulting current compensation of the dc-link currents leads to a reduced load on the dc-link capacitor and the HV-dc-grid (see [1]). Based on this, the foundation for an optimized design of the dc-link capacitor and a real-time capable determination of the ideal switching cycle shift is created. The downsizing of the dc-link capacitor, which is enabled according to [14], creates a potential for reducing costs, weight, and volume.

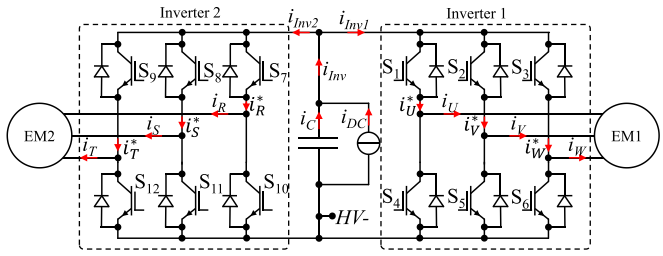

Fig. 1. Topology and important signals of the considered dual-inverter.

II. Definition and Parameter Introduction

Fig. 1 shows the topology of the dual-inverter on which the following explanations rely. As mentioned, the operating points of the two electrical motors and thus of the two inverters are independent from each other. The two inverters are connected to a common dc-link. The dual-inverter is supplied by a current source. Its current I_{DC} can be understood as a pure dc signal. The capacitor current I_C is a pure ac signal and is defined as follows:

$$I_C = I_{\mathrm{Inv}} - I_{\mathrm{DC}}. \tag{1}$$

The dc-link current I_{Inv} is composed of the dc-link currents of the two inverters according to the following:

$$I_{\mathrm{Inv}} = I_{\mathrm{Inv1}} + I_{\mathrm{Inv2}}. \tag{2}$$

The dc-link current of Inverter1 results, as defined in the following, from the sum of the switch currents I_U^*, I_V^*, and I_W^*:

$$I_{\mathrm{Inv1}} = I_U^* + I_V^* + I_W^*. \tag{3}$$

Similarly, the dc-link current of Inverter2 can be defined by the following:

$$I_{\mathrm{Inv2}} = I_R^* + I_S^* + I_T^*. \tag{4}$$

During the time segments in which either the upper diode or the upper IGBT of phase U conducts, the phase current I_U, and the switch current I_U^* are identical. Otherwise, the switch current I_U^* equals 0. The same applies to the relationships between the switch and phase currents of the phases V, W, R, S, and T. The control signals $s_1(t)$ to $s_{12}(t)$ of the switches S_1 to S_{12} can be understood to be logical functions, which equal 1 in case their IGBT or diode conducts. For blocking time periods, these equal 0. Thus, the switch current can be defined as a function of the phase current, as presented as follows:

$$i_U^*(t) = i_U(t) \cdot s_1(t). \tag{5}$$

The relationship between switch current, phase current of phase U, and the control function of S_1, as shown in (5), can be used in the same way for the switch currents of the other phases. The control functions $s_1(t)$ to $s_{12}(t)$ are dependent on the applied modulation strategy. In the following explanations, space-vector modulation (SVM) is taken into account as defined in [15]. The time functions of the phase currents of Inverter1 are defined as follows:

$$i_U(t) = \hat{I}_{UVW} \cdot \cos(\omega_{f1} t - \varphi_1) \tag{6}$$

$$i_V(t) = \hat{I}_{UVW} \cdot \cos\left(\omega_{f1}t - \varphi_1 + \frac{2\pi}{3}\right) \quad (7)$$

$$i_W(t) = \hat{I}_{UVW} \cdot \cos\left(\omega_{f1}t - \varphi_1 + \frac{4\pi}{3}\right). \quad (8)$$

Here, $\hat{I}_{UVW}$ is the amplitude of the phase currents from Inverter1. The fundamental angular frequency is defined as $\omega_{f1} = 2\pi f_{f1}$, where f_{f1} represents the fundamental frequency of the phase current of Inverter1. The angle φ_1 represents the shift between the fundamental waves of phase voltage and phase current of Inverter1. If the pulse width of the switch signal $s_1(t)$ is normalized to the switching period, the time function, shown as follows, results for the first two sectors:

$$\gamma_1(t) = \rho + (\rho - 1)\frac{\sqrt{3}}{2}M_1 \sin\left(\omega_{f1}t + \frac{4\pi}{3}\right) \quad \text{for } 0 \le t \le \frac{\pi}{3\omega_{f1}} \quad (9)$$

$$\gamma_1(t) = \rho + \rho\frac{\sqrt{3}}{2}M_1 \sin(\omega_{f1}t + \pi) + \frac{\sqrt{3}}{2}M_1 \sin\left(\omega_{f1}t + \frac{\pi}{3}\right) \quad \text{for } \frac{\pi}{3\omega_{f1}} \le t \le \frac{2\pi}{3\omega_{f1}}. \quad (10)$$

Equations (9) and (10) are based on the time definitions of the switching states for SVM as explained in [5], [6], and [15]. The variable ρ regulates the division of how long which of the two zero pointers is used in the corresponding sector. Since SVM is considered in this publication, ρ can be assumed constantly as 0.5. This parameter would have to be adjusted for the analysis of discontinuous modulation strategies. The variable M_1 represents the modulation index of Inverter1 and is defined according to the following:

$$M_1 = \frac{\hat{V}_{U\_HV-}}{\frac{V_{DC}}{2}}. \quad (11)$$

The signal $\hat{V}_{U\_HV-}$ stands for the fundamental wave amplitude of the voltage between phase U and *HV*–. Since both electrical motors can be operated independently, their speeds and thus their electrical fundamental waves are not necessarily identical. Therefore, the signals from Inverter2 have an own fundamental angular frequency $\omega_{f2} = 2\pi f_{f2}$. Even if the rotating field frequency of Inverter1 and Inverter2 is identical, it must not necessarily be assumed an in-phase scenario. Due to this aspect, the normalized switch signals from Inverter2 are shifted to those from Inverter1 by the angle β. The switch signal of switch S_7 normalized to the switching period for the first two sectors can be taken from the following:

$$\gamma_7(t) = \rho + (\rho - 1)\frac{\sqrt{3}}{2}M_2 \sin\left(\omega_{f2}t + \beta + \frac{4\pi}{3}\right) \quad \text{for } \frac{0-\beta}{\omega_{f2}} \le t \le \frac{\pi - \beta}{3\omega_{f2}} \quad (12)$$

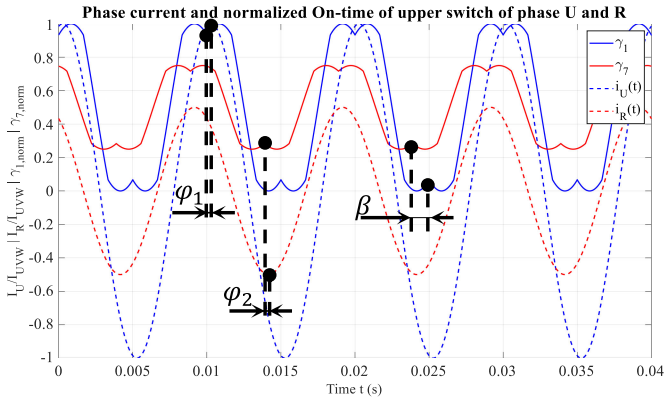

Fig. 2. Phase current and normalized On-time of upper switch of phase *U* and *R* at the following operating point: $\hat{I}_{RST} = \hat{I}_{UVW}/2$, $f_{f1} = f_{f2} = 100$ Hz, $\varphi_1 = \pi/18$, $\varphi_2 = \pi/18$, $\beta = 2\pi/9$, $M_1 = 2/\sqrt{3}$, $M_2 = 1/\sqrt{3}$.

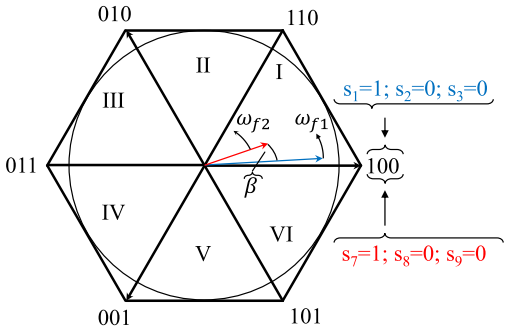

Fig. 3. Exemplary illustration of Inverter1's and Inverter2's voltage vectors in SVM's hexagon.

$$\gamma_7(t) = \rho + \rho\frac{\sqrt{3}}{2}M_2 \sin(\omega_{f2}t + \beta + \pi) + \frac{\sqrt{3}}{2}M_2 \sin\left(\omega_{f2}t + \beta + \frac{\pi}{3}\right) \quad \text{for} \frac{\pi}{3\omega_{f2}} \le t \le \frac{2\pi}{3\omega_{f2}}. \quad (13)$$

The variable M_2 represents the modulation index of Inverter2 and is defined analogously to (11). Furthermore, the time functions shown as follows can be derived for the phase currents of Inverter2:

$$i_R(t) = \hat{I}_{RST} \cdot \cos(\omega_{f2}t - \varphi_2 + \beta) \quad (14)$$

$$i_S(t) = \hat{I}_{RST} \cdot \cos\left(\omega_{f2}t - \varphi_2 + \frac{2\pi}{3} + \beta\right) \quad (15)$$

$$i_T(t) = \hat{I}_{RST} \cdot \cos\left(\omega_{f2}t - \varphi_2 + \frac{4\pi}{3} + \beta\right). \quad (16)$$

The definition of the angles φ_1 and φ_2 as well as the fundamental wave shift β are illustrated in Fig. 2 based on the exemplary time functions. In Fig. 3, β is explained again using the voltage vectors of Inverter1 and Inverter2 in the hexagon of the SVM. The fundamental wave shift cannot be influenced usually. In the case of traction inverters, it is defined by the

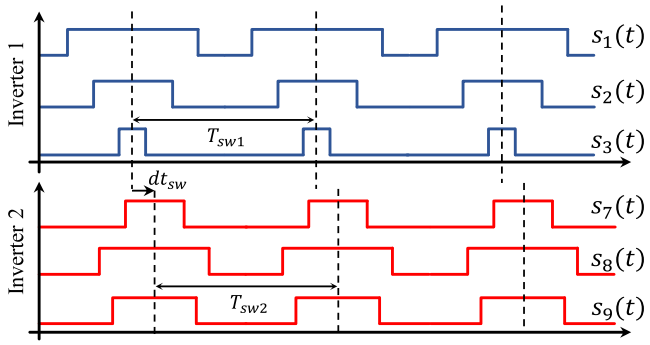

Fig. 4. Example of a dual-inverter's control signals with a $dt_{\mathrm{sw}} > 0$ and therefore a $\sigma > 0$.

driving situation and the resulting rotor positions of the electric motors. However, the switching cycle shift σ has no influence on the behavior of the electrical motors. It represents a degree of freedom in controlling the dual-inverter and has a significant influence on the frequency spectrum and the rms value of I_{Inv}. The switching cycle shift is the angle between the control signals from Inverter1 and Inverter2. According to (17), this is derived from the time shift of the control signals

$$\sigma = \frac{dt_{\mathrm{sw}}}{T_{\mathrm{sw2}}} \cdot 2\pi. \tag{17}$$

Here, dt_{sw} is the time shift of the switching signals from Inverter1 to Inverter2 and T_{sw2} is the switching period of Inverter2. Fig. 4 illustrates an example of control functions of the dual-inverter with $\sigma > 0$. The dashed lines mark the middle of the switching periods of Inverter1 and Inverter2.

III. Analytic Spectrum Calculation

A. Description of the Current Spectrum as an Integral Function

As explained in [7], the spectrum of the dc-link current of a single-inverter results from the sum of the spectra of the three switch currents. In relation to the topology shown in Fig. 1, this approach can be assigned to I_{Inv1}, shown as follows:

$$I_{\mathrm{Inv1}}(f) = I_U^*(f) + I_V^*(f) + I_W^*(f). \tag{18}$$

In order to describe the spectra of the switch currents, the method of the geometric wall model is used [7]. Instead of generating the Fourier integral over the switch current time function (5) of phase U, the spectrum of the switch current can be expressed by a double Fourier integral over the phase current of phase U. Using this method, the control function $s_1(t)$, which is part of (5), is then transferred into the integration limits of the inner integral. The spectrum of the switch current of phase U is indicated as follows:

$$I_U^*(f) = \frac{1}{2\pi^2} \cdot \hat{I}_{UVW} \cdot \sum_{i=1}^{6} \int_{y_s(i)}^{y_e(i)} \int_{x_r(i)}^{x_f(i)} \cos(y-\varphi_1) \cdot e^{j(m\cdot x + n\cdot y)} dx\, dy. \tag{19}$$

TABLE I
Integration Limits for Double-Fourier Integral of Switch Current of Phase U

i	$y_s(i)$	$y_e(i)$	$x_r(i)$	$x_f(i)$
1	0	$\frac{\pi}{3}$	$\pi - \frac{\gamma_U}{2}$, with $\gamma_1 \rightarrow$ (9)	$\pi + \frac{\gamma_U}{2}$, with $\gamma_1 \rightarrow$ (9)
2	$\frac{\pi}{3}$	$\frac{2\pi}{3}$	$\pi - \frac{\gamma_U}{2}$, with $\gamma_1 \rightarrow$ (10)	$\pi + \frac{\gamma_U}{2}$, with $\gamma_1 \rightarrow$ (10)

Here, x and y result from the substitution shown as follows:

$$x = \omega_{sw1} \cdot t \tag{20}$$

$$y = \omega_{f1} \cdot t. \tag{21}$$

The variables y_s, y_e, x_r, and x_f form the integration limits of the inner and outer integral. Furthermore, the relationship between m, n, and frequency f is defined as follows:

$$f = \frac{1}{2\pi} \cdot (m \cdot \omega_{sw1} + n \cdot \omega_{f1}), \text{ with } m,\ n \in \mathbb{N}. \tag{22}$$

To get an analytical spectrum of the switch current, all six sectors of the hexagon are integrated. However, the integration over two sectors is sufficient for the spectrum $I_{\mathrm{Inv1}}(f)$, since this signal has a $2\pi/3$-periodicity according to [5], [6], [11]. For this reason, the functions $I_U^{\sim}$, $I_V^{\sim}$, and $I_W^{\sim}$ are introduced.

$$I_{\mathrm{Inv1}}(f) = I_U^{\sim}(f) + I_V^{\sim}(f) + I_W^{\sim}(f). \tag{23}$$

The function $I_U^{\sim}$ is defined according to the following:

$$I_U^{\sim}(f) = \frac{1}{2\pi^2} \cdot \hat{I}_{UVW} \cdot \sum_{i=1}^{2} \int_{y_s(i)}^{y_e(i)} \int_{x_r(i)}^{x_f(i)} \cos(y-\varphi_1) \cdot e^{j(m\cdot x + n\cdot y)} dx\, dy. \tag{24}$$

The associated integration limits can be found in Table I. With (18), (24) and the associated integration limits, the spectrum of the current $I_{\mathrm{Inv1}}(f)$ can be determined, now. However, this is only possible using numerical integration of the outer integral. A solved form of the spectrum and its derivation is presented as follows. For this purpose, the inner integral of (24) is solved. This results in the expression shown as follows:

$$I_U^{\sim}(f) = \frac{1}{2\pi^2} \cdot \hat{I}_{UVW} \cdot \sum_{i=1}^{2} \int_{y_s(i)}^{y_e(i)} \cos(y-\varphi_1) \cdot e^{jyn} \cdot \left[-\frac{j}{m} \cdot e^{jxm} \right]_{x_r(i)}^{x_f(i)} dy. \tag{25}$$

If the integration limits from Table I are used in (25), the definition shown in (26) bottom of this page, can be derived.

According to [15], the expressions given in (26) are elementary integrals, which cannot be solved in closed form. In order to achieve a solved description of the spectrum, an approximate solution is determined using the Newton–Cotes formulas as defined in [16]–[19].

B. Solution of the Outer Integral by Newton–Cotes

As explained, a closed solution of the integrals from (26) is not possible. However, the Newton–Cotes formulas can be used to generate a highly accurate approximation. The Newton–Cotes formulas are numerical quadrature formulas for the approximate determination of an antiderivative of a function. They are based on the idea of interpolating the original function by the use of a polynomial. Then, for the integral of the resulting function, an exact solution can be generated. Within the considered area, the locations of the required sampling points are in equidistant intervals. Their successful application for double Fourier integrals has already been demonstrated in [20] and [21]. The closed Newton–Cotes formulas such as Weddle rule, Simpson rule, or Pulcherima rule differ in the number of sampling points and their weights. The Weddle rule, for instance, is based on six sampling points. The Pulcherima rule, also known as 3/8-rule, is based on four sampling points. For the solution of (26), both the Simpson rule and the Pulcherrima (3/8 rule) as defined in [16]–[19] have been considered. This analysis showed that the 3/8 rule delivers a significantly more compact result with slightly lower accuracy. Hence, the results based on the 3/8 rule are presented as follows. For this, the function to be integrated from (25) is first substituted, shown as follows:

$$A\left(y\right)=\cos\left(y-\varphi_1\right)\cdot e^{jyn}\cdot\left[-\frac{j}{m}\cdot e^{jxm}\right]_{x_r(i)}^{x_f(i)}. \tag{27}$$

Applying the 3/8 rule results in the expression shown as follows:

$$\sum_{i\,=\,1}^{2}\int_{y_{s(i)}}^{y_{e(i)}}A\left(y\right)dy\approx\sum_{i\,=\,1}^{2}\int_{y_{s(i)}}^{y_{e(i)}}B\left(y\right)dy=\sum_{i=1}^{2}\times\left(y_{e(i)}-y_{s(i)}\right)\cdot\sum_{k=1}^{4}w_k\cdot A\left(d_k\right). \tag{28}$$

Here, $B(y)$ represents the function approximated to the original function. The coefficient w_k represents the weights. This can be found in Table II. The coefficient d_k describes the location of the steps and is defined as follows:

$$d_k=y_s\ +c_k\cdot\left(y_e-y_s\right). \tag{29}$$

TABLE II
WEIGHT AND NORMALIZED LOCATION OF SAMPLING POINT

k	1	2	3	4
w_k	$\frac{1}{8}$	$\frac{3}{8}$	$\frac{3}{8}$	$\frac{1}{8}$
c_k	0	$\frac{1}{3}$	$\frac{2}{3}$	1

According to [16]–[19], four reference points have to be used for the 3/8 rule. Hence, $k\in\{1,\ 2,\ 3,\ 4\}$ applies for the index. The variable c_k represents the normalized location of the steps, which can also be found in Table II. With (26)–(29) and Table II the solution (A1) for $I_U^{\sim}(f)$, shown in the appendix, can be derived. This solution does not contain any integral or differential expressions. Similarly, $I_V^{\sim}$ and $I_W^{\sim}$ can be described by (A2) and (A3) given in the appendix. According to (23) the spectrum $I_{\mathrm{Inv1}}(f)$ results from the sum of (A1), (A2), and (A3).

C. Derivation of the Total Spectrum of the Dual-Inverter

As explained in Fig. 2, the normalized switch functions γ_1 and γ_7 are shifted by the angle β. This becomes transparent in the comparison of their time functions (9) and (12). In addition, the control signals from Inverter2 are shifted by σ to the signals from Inverter1. Analogous to the representation of $I_U^{\sim}(f)$ from (24), the description of $I_R^{\sim}(f)$ can be derived. It is given as follows:

$$I_R^{\sim}\ (f)=\frac{1}{2\pi^2}\ \cdot\hat{I}_{RST}\cdot e^{j(g\cdot\sigma-h\cdot\beta)}\cdot\sum_{i\,=\,1}^{2}\int_{y_s(i)}^{y_e(i)}\int_{x_r(i)}^{x_f(i)}\cos\left(y-\varphi_2\right)\cdot e^{j(g\cdot x+h\cdot y)}dx\ dy. \tag{30}$$

The two variables x and y are defined according to (31) and (32), respectively. The variables g and h define the frequency f as shown as follows:

$$x\ =\omega_{sw2}\ \cdot t \tag{31}$$

$$\begin{aligned}I_U^{\sim}\left(f\right)=\frac{1}{2\pi^2}\cdot\hat{I}_{UVW}\cdot\Bigg(&\int_0^{\frac{\pi}{3}}-\cos\left(y-\varphi_1\right)\cdot e^{jyn}\cdot e^{j\cdot m\cdot\left(\frac{3\pi}{2}-\frac{\pi}{2}\cdot\frac{\sqrt{3}}{2}\cdot M_1\cdot\sin\left(y+\frac{4\pi}{3}\right)\right)}\cdot\frac{j}{m}\\&+\cos\left(y-\varphi_1\right)\cdot e^{jyn}\cdot e^{j\cdot m\cdot\left(\frac{\pi}{2}+\frac{\pi}{2}\cdot\frac{\sqrt{3}}{2}\cdot M_1\cdot\sin\left(y+\frac{4\pi}{3}\right)\right)}\cdot\frac{j}{m}\,dy\\&+\int_{\frac{\pi}{3}}^{\frac{2\pi}{3}}-\cos\left(y-\varphi_1\right)\cdot e^{jyn}\cdot e^{j\cdot m\cdot\left(\frac{3\pi}{2}+\frac{\pi}{2}\cdot\frac{\sqrt{3}}{2}\cdot M_1\cdot\sin(y+\pi)+\pi\frac{\sqrt{3}}{2}\cdot M_1\sin\left(y+\frac{\pi}{3}\right)\right)}\cdot\frac{j}{m}\\&+\cos\left(y-\varphi_1\right)\cdot e^{jyn}\cdot\ e^{j\cdot m\cdot\left(\frac{\pi}{2}-\frac{\pi}{2}\cdot\frac{\sqrt{3}}{2}\cdot M_1\cdot\sin(y+\pi)-\pi\frac{\sqrt{3}}{2}\cdot M_1\sin\left(y+\frac{\pi}{3}\right)\right)}\cdot\frac{j}{m}\,dy\end{aligned} \tag{26}$$

$$y = \omega_{f2} \cdot t \tag{32}$$

$$f = \frac{1}{2\pi} \cdot (g \cdot \omega_{sw2} + h \cdot \omega_{f2}). \tag{33}$$

If (30) is solved according to the procedure explained for phase U, the expression (A4) shown in the Appendix results in $I_R^{\sim}(f)$. The expressions of (A1) and (A4) are identical in their form and only differ in the multiplication factor $e^{j(g\sigma - h\beta)}$. Therefore, the functions $I_R^{\sim}(f)$, $I_S^{\sim}(f)$ and $I_T^{\sim}(f)$ can be derived from (A1), (A2), and (A3) as explained in (34), (35), and (36), respectively

$$I_U^{\sim}(f) \overset{\hat{I}_{UVW}\to\hat{I}_{RST};\ m\to g;\ n\to h;\ M_1\to M_2;\ \varphi_1\to\varphi_2;\ 1\to e^{j(g\sigma-h\beta)}}{\to} I_R^{\sim}(f) \tag{34}$$

$$I_V^{\sim}(f) \overset{\hat{I}_{UVW}\to\hat{I}_{RST};\ m\to g;\ n\to h;\ M_1\to M_2;\ \varphi_1\to\varphi_2;\ 1\to e^{j(g\sigma-h\beta)}}{\to} I_S^{\sim}(f) \tag{35}$$

$$I_W^{\sim}(f) \overset{\hat{I}_{UVW}\to\hat{I}_{RST};\ m\to g;\ n\to h;\ M_1\to M_2;\ \varphi_1\to\varphi_2;\ 1\to e^{j(g\sigma-h\beta)}}{\to} I_T^{\sim}(f). \tag{36}$$

The spectrum of the current $I_{\mathrm{Inv}2}$ is defined as follows:

$$I_{\mathrm{Inv}2}(f) = I_R^{\sim}(f) + I_S^{\sim}(f) + I_T^{\sim}(f). \tag{37}$$

According to (2), (23), and (37), the sum of (A1)–(A3) and (34)–(36), then defines the total spectrum $I_{\mathrm{Inv}}(f)$. In case of asymmetrical current amplitudes in the phases of the two electrical motors, the amplitudes $\hat{I}_{UVW}$ and $\hat{I}_{\mathrm{RST}}$ in (A1)–(A4), as well as in (35) and (36), can be replaced by $\hat{I}_U, \hat{I}_V, \hat{I}_W, \hat{I}_R, \hat{I}_S$, and $\hat{I}_T$. These represent the individual current amplitudes in the respective phases. Here, the relevant definitions in (A1)–(A4), (35) and (36), as well as the relationship shown in (37) remain valid.

IV. Analytic RMS-Current Calculation

The description of the approximate rms value of the current I_C and its derivation are explained as follows. Since the rms value of the dc-link current has to be derived as a function of the switching cycle shift σ, the methods used in [5] and [6] cannot be applied. Therefore, a new approach has to be deduced. The basis for this is the analytic description of the frequency spectrum $I_{\mathrm{Inv}}(f)$, which has been presented previously. As mentioned above, I_{DC} can be understood as a pure dc-signal. According to (1) it can be concluded that I_C corresponds to the ac component of I_{Inv}. Since the Fourier series describes a signal as the sum of angle functions with corresponding Fourier coefficients [22], the relationship shown as follows can be deduced:

$$i_C(t) = \sum_{k=1}^{\infty} Re\{I_{\mathrm{Inv}}(f_k)\} \cdot \cos(2\pi f_k \cdot t) + Im\{I_{\mathrm{Inv}}(f_k)\} \cdot \sin(2\pi f_k \cdot t). \tag{38}$$

The frequencies at which the highest spectrum amplitudes of a single-inverter $I_{\mathrm{Inv1}}(f)$ occur are known from the results published in [7] and [14]. These are the harmonics of the switching frequency and their sidebands. In the case of odd harmonics, the sidebands are around $\pm 3f_f$ and for even harmonics they occur around $\pm 6f_f$. An approximate description of the rms value, which takes into account the first six harmonics and their sidebands, is defined as (39) shown at bottom of this page.

Here, the variable f is a function of m and n, as determined in (22). According to Parseval's theorem, the energy of a time signal is equal to the energy of its spectrum. The following equation is derived from this law:

$$\frac{1}{T_{ic}} \int_0^{T_{ic}} [|i_C(t)|]^2 dt = \sum_{k=1}^{\infty} |I_{\mathrm{Inv}}(f_k)|^2. \tag{40}$$

T_{ic} represents the period of the current time function $i_C(t)$. Thus, the averaged integral of the squared time function is equivalent to the integral of the squared spectrum. Based on this correlation, the approximate arithmetic mean value of the capacitor current can be described as (41) shown at the bottom of this page.

The expression defined in (41) represents the approximate $I_{C,\mathrm{RMS}}$ of the dual-inverter. Therefore, it can be understood as a counterpart to the $I_{C,\mathrm{RMS}}$ of the single-inverter, specified in [5] and [6].

V. Verification of the Results Through Simulation and Calculation

The following section examines the validity of the results presented in Sections III and IV based on simulations and calculations. The simulation data are generated using a MATLAB model. This generates the time function of the switch signals with a step size of 10 ns and a switching frequency of 10 kHz.

$$i_C(t) \approx \sum_{n\in\{-3;0;3\}} \sum_{m\in\{1;3;5\}} Re\{I_{\mathrm{Inv}}(f)\} \cdot \cos(2\pi f \cdot t) + Im\{I_{\mathrm{Inv}}(f)\} \cdot \sin(2\pi f \cdot t) + \sum_{n\in\{-6;0;6\}} \sum_{m\in\{2;4;6\}} Re\{I_{\mathrm{Inv}}(f)\} \cdot \cos(2\pi f \cdot t) + Im\{I_{\mathrm{Inv}}(f)\} \cdot \sin(2\pi f \cdot t) \tag{39}$$

$$I_{C,\mathrm{RMS}} \approx \sqrt{\left[\sum_{n\in\{-3;0;3\}} \sum_{m\in\{1;3;5\}} [|I_{\mathrm{Inv}}(f)|]^2 + \sum_{n\in\{-6;0;6\}} \sum_{m\in\{2;4;6\}} [|I_{\mathrm{Inv}}(f)|]^2\right]} \tag{41}$$

The phase currents are considered as ideal cosine functions. This is realized by the use of a cosine current source for each motor phase. Thereby, no further dc- supply is required for the simulation. The switch currents and thus the dc-link currents I_{Inv1}, I_{Inv2}, and I_{Inv} are calculated from this. The validity of this simulation method has been proven by measurement in [14]. The contents explained and verified in [5]–[7] form the basis for the verifications by calculation, which are presented as follows. In order to achieve a clear graphical representation of the results, the modulation degrees of Inverter1 and Inverter2 are normalized to a maximum of 1. The normalized modulation indices are represented by M_{PhPh1} and M_{PhPh2} specified in (42) and (43). They result from the ratio of the fundamental wave amplitude of the phase–phase voltages to the dc voltage of the dc-link capacitor.

$$M_{\mathrm{PhPh1}} = M_1 \cdot \frac{\sqrt{3}}{2} \tag{42}$$

$$M_{\mathrm{PhPh2}} = M_2 \cdot \frac{\sqrt{3}}{2}. \tag{43}$$

A. Verification of the Newton–Cotes Based Solution by Calculation

As explained in Section III, the sum of (A1)–(A3) represents the analytical description of the approximate frequency spectrum of I_{Inv1}. Equation (24) defines the original function, verified in [6], as a double Fourier integral. The high accuracy of the description of the dc-link current spectrum presented in this article becomes obvious in Fig. 5. This shows the magnitude of the dc-link current I_{Inv1} as a function of M and $\cos(\varphi)$ for different frequencies. Fig. 5(a) is generated based on the analytical solved form, which is described in Section III. Fig. 5(b) is calculated by (24), which is verified according to [6], [13]. The approximate identical results of the two illustrations prove the validity of the presented solution using Newton–Cotes.

B. Verification of the Dual-Inverter Spectrum by Simulation

According to (23), the spectrum of the dc-link current I_{Inv1} is defined by the sum of the upper switch current spectra of Inverter1. Similarly, (37) defines the spectrum of the current I_{Inv2} by the sum of the upper switch current spectra of Inverter2. In order to obtain the total dc-link current I_{Inv}, all upper switch current spectra of both inverters have to be summarized. As a result of the fundamental wave shift β and the switching cycle shift σ, the spectrum of I_{Inv2} is shifted to the spectrum of I_{Inv1} by the multiplication factor $e^{j(g\sigma - h\beta)}$. The validity of the solved form of the spectrum $I_{\mathrm{Inv}}(f)$ is demonstrated as follows. For this purpose, an exemplary operating point of the two electrical motors is taken into account, which remains constant. Only the fundamental wave shift and the switching cycle shift are varied. Here, the magnitude of the spectrum $I_{\mathrm{Inv}}(f)$ for the exemplary frequency $f = f_{\mathrm{sw}} \pm 3 \cdot f_f$ is considered. Fig. 6(a) shows the magnitude, which results from the sum of (A1)–(A4) and the analogously generated spectra $I_V^{\sim}(f)$ and

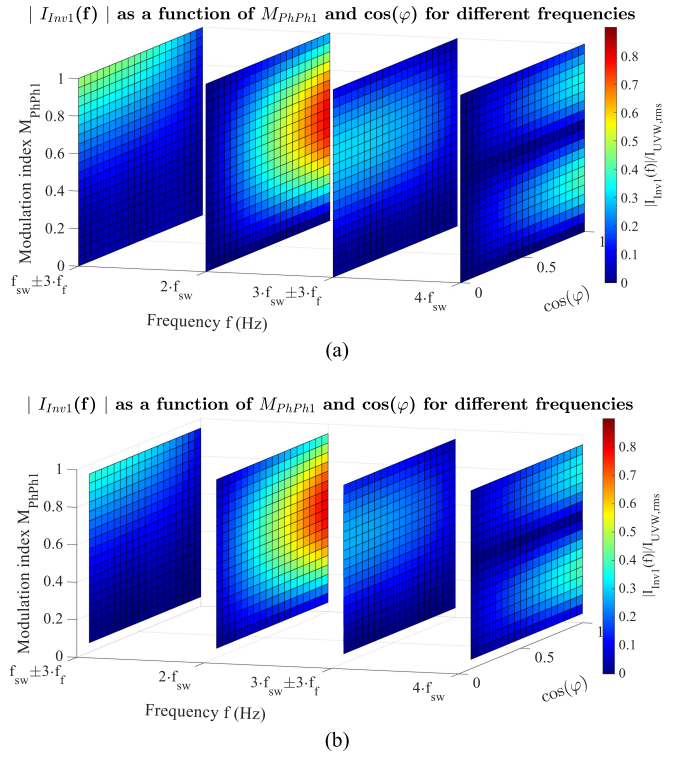

Fig. 5. (a) DC-link current harmonic simulation for SVM based on Newton–Cotes-solution. (b) Harmonics calculated by double-Fourier-integral.

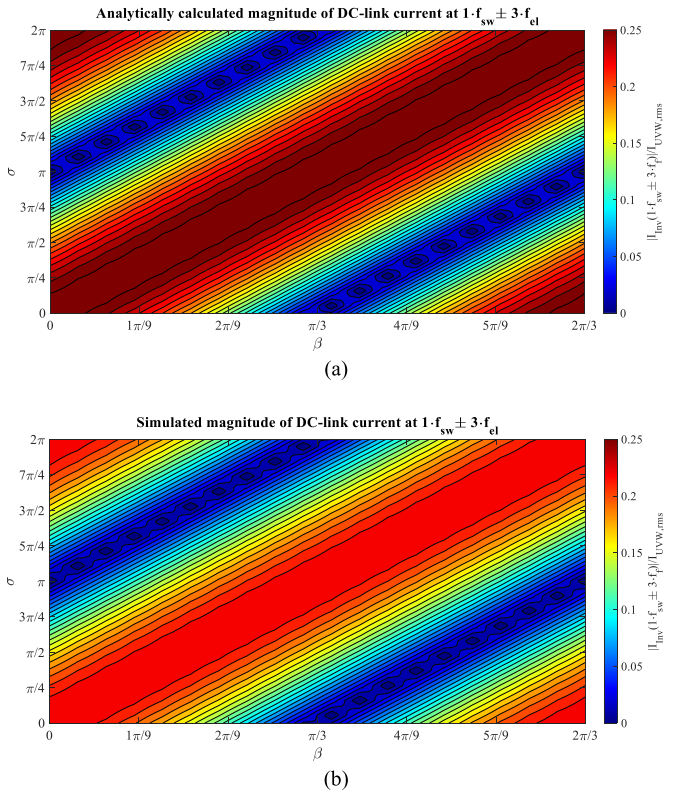

Fig. 6. Magnitude of $I_{Zk}(f)$ at $f = f_{\mathrm{sw}} \pm 3 \cdot f_f$ as a function of σ and β. Considered operating point: $I_{\mathrm{UVW}} = I_{\mathrm{RST}}$, $M_1 = M_2 = 0,5$, $\varphi_1 = \varphi_2 = \pi/3$, $f_{f1} = f_{f2} = 200$ Hz. (a) Analytically calculated. (b) Simulated.

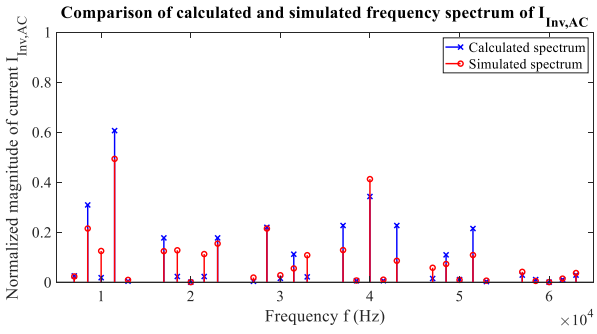

(a)

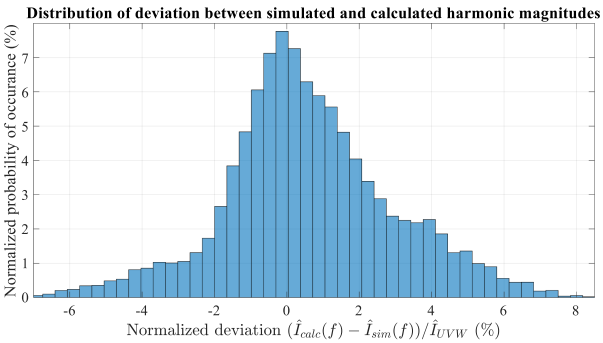

(b)

Fig. 7. (a) Comparison of the calculated and simulated frequency spectrum of $I_{\mathrm{Inv,AC}}$ for the following operating point: $I_{\mathrm{UVW}} = I_{\mathrm{RST}} = 1\mathrm{A}$, $f_{f1} = f_{f2} = 500\,\mathrm{Hz}$, $\cos(\varphi_1) = \cos(\varphi_2) = 0.6$, $\beta = 8\pi/5$, $M_1 = M_2 = 0.9$, $\sigma = \pi/2$. (b) Normalized deviation $(\hat{I}_{calc}(f) - \hat{I}_{sim}(f))/\hat{I}_{UVW}$ for six harmonic frequencies ($f \in \{f_{sw}; 3 \cdot f_f + f_{sw}; 2 \cdot f_{sw}; 6 \cdot f_f + 2 \cdot f_{sw}; 3 \cdot f_{sw}; 3 \cdot f_f + 3 \cdot f_{sw}\}$) of 5^6 operating points.

$I_{\tilde{W}}(f)$. The magnitude shown in Fig. 6(b) results from the MATLAB model that has been mentioned in the beginning of this section. A comparison of the two graphics reveals a slight discrepancy between the magnitudes of Fig. 6(a) and (b). The qualitative development of the calculated magnitude over σ and β is in line with the simulation. Therefore, the validity of the prefactor $e^{j(g\sigma - h\beta)}$, as well as the definition of the total spectrum $I_{\mathrm{Inv}}(f)$ in solved form can be considered as proven. In order to check the validity of the calculation of the spectrum with regard to further operating points at other frequencies, Fig. 7(a) shows a comparison of the simulated and calculated spectrum for a specific operating point. Here, the good correlation of the calculated values with the simulated results can be seen, too. Furthermore, the overall operating area is investigated by a random selection of operating points. The variables M_1, M_2, φ_1, φ_2, σ, and β define an operating area. From this operating area, $5^6 = 15625$ operating points are selected randomly. The fundamental frequencies are kept constant at 200 Hz. For f_{sw1} and f_{sw2} a frequency of 10 kHz is taken into account. For each of the considered operating points, the amplitudes of the harmonics of six frequencies ($f \in \{f_{\mathrm{sw}}; 3 \cdot f_f + f_{\mathrm{sw}}; 2 \cdot f_{\mathrm{sw}}; 6 \cdot f_f + 2 \cdot f_{\mathrm{sw}}; 3 \cdot f_{\mathrm{sw}}; 3 \cdot f_f + 3 \cdot f_{\mathrm{sw}}\}$) are calculated and simulated. The deviations between the calculated and the simulated values are normalized to the phase current amplitude. This deviations and their probability of occurrence are presented in Fig. 7(b). According to this investigation, the probability of a calculated result with an error $<1\%$ is approximately 45%. The probability of a calculated result with an error $<4\%$ is already around 88%.

C. Verification on the Example of the Calculated Single-Inverter RMS DC-Link Current

According to (1), the capacitor current I_C is equal to the ac-component of the current I_{Inv}. The relation between the rms value of the capacitor current and its spectrum is defined in (40). According to (41), the rms value of this current can be approximated by its spectral components with highest magnitudes. The correctness of the relationship defined in (41) is examined as follows. The analytic equation (44) of the rms-value of the dc-link current as a function of M and $\cos(\varphi)$, as defined and validated in [5] and [6], is used as a reference for this.

$$I_{C,\mathrm{rms}} = \hat{I}_{UVW} \cdot \sqrt{\frac{\sqrt{3} \cdot M}{4\pi} + \left(\frac{\sqrt{3} \cdot M}{\pi} - \frac{9 \cdot M^2}{16}\right) \cdot \cos^2(\varphi)}\,. \tag{44}$$

This definition represents the capacitor current of a single-inverter. Therefore, it is compared with the definition of the ac rms value of I_{Inv1} according to the approximation method explained in (41). The Fourier coefficients used here are calculated by the expressions explained in (23) and (A1)–(A3). Fig. 8 shows the rms value of the ac-component of I_{Inv1} as a function of M and $\cos(\varphi)$. Here, Fig. 8(a) illustrates the analytical solution of the current, which is described in Sections III and IV. The current shown in Fig. 8(b) is generated using expression (44), which is defined in [5] and [6]. The high accuracy of the approximation presented in this article is pointed out in Fig. 8. A noteworthy deviation between the novel calculation method from Fig. 8(a) and the values shown in Fig. 8(b) results for high power factors combined with high modulation indices. In this area, the presented spectrum-based method provides slightly lower rms values. Further investigations based on the trapezoidal rule defined in [16]–[19] with an increased number of steps has been carried out. In addition, further harmonics and sidebands have been taken into account. These considerations showed an improved accuracy. However, this improvement is associated with a disproportionately higher calculation and computational effort.

VI. Metrological Verification

Based on the measurement of a dual-inverter, the accuracy of $I_{C,\,\mathrm{rms}}$ derived by (41) is examined as follows. The device under test is a traction inverter with a maximum dc operating voltage rating of 800 V and a maximum rms phase current rating of 600 A. It is based on a two-level topology. As part of

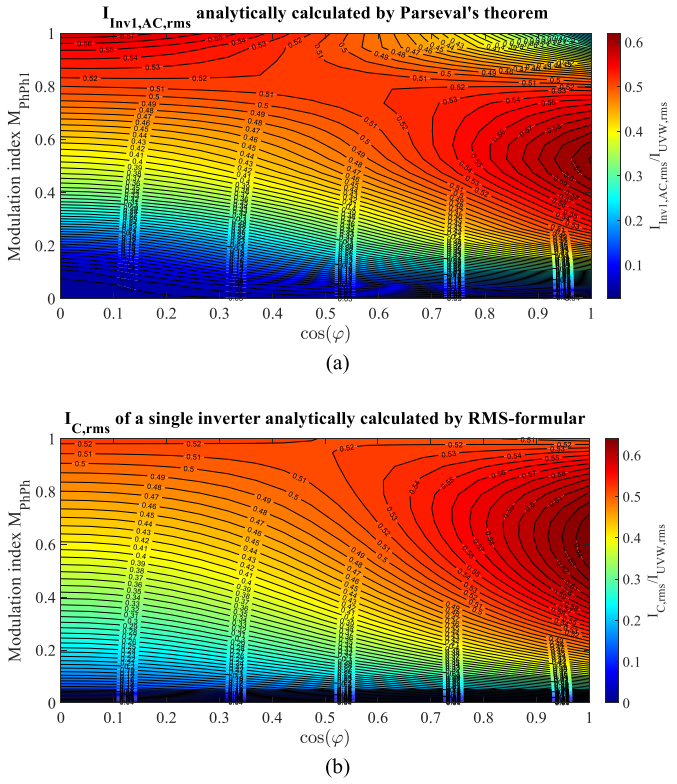

Fig. 8. RMS-current $I_{\mathrm{Inv1,AC,rms}}$ as a function of M_{PhPh} and $\cos(\varphi)$. (a) Analytically calculated by Parseval's theorem. (b) Analytically calculated by (44).

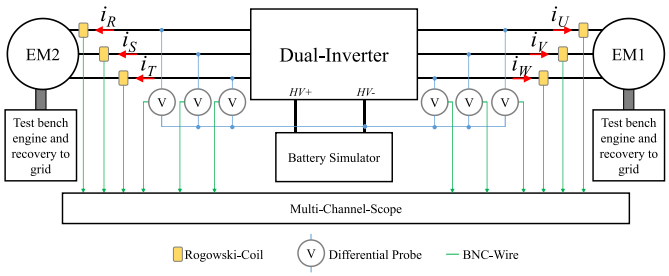

Fig. 9. Measurement setup and recorded signals.

the metrological verification, two three-phase electrical motors have been driven by the dual-inverter. The operating point of the dual-inverter has been set by its control and the generators used. The device has been supplied by a battery simulator. The three voltages between the phase connections and HV–, as well as the three phase currents per motor, have been fed to the multichannel scope Yokogawa DL850. A sampling rate of 1 MS/s has been used. The current measurement has been implemented by Rogowski coils. All voltages have been measured using differential probes. A dc voltage of 400 V has been applied for the measurement. The used measurement setup is shown in Fig. 9. Based on the measured voltages between the phases of the inverter and HV–, the time periods with conductive upper switches have been

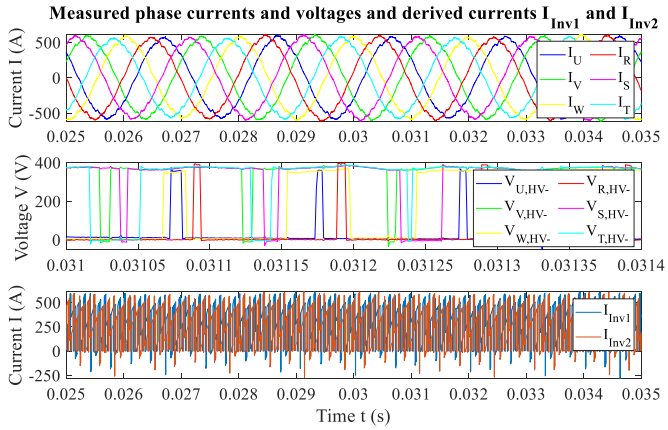

Fig. 10. Measured signals for an exemplary operating point and derived dc-link currents of the two subinverters. $\hat{I}_{\mathrm{UVW}} \approx \hat{I}_{\mathrm{RST}} \approx 590$ A, $f_{f1} \approx f_{f2} = 500$ Hz, $\cos(\varphi_1) = 0.58$, $\cos(\varphi_2) = 0.56$, $\beta = 5.55$, $M_1 \approx M_2 \approx 0.89$, $\sigma = \frac{\pi}{2}$; $T = 100$ N·m.

extracted. By combining this information with the measured phase currents, the switch currents can be derived analogously to the procedureexplained in [14]. The sum of the upper switch currents of a subinverter represents its dc-link current. Fig. 10 presents the phase currents, the voltages between the phase connections and HV–, and the derived currents I_{Inv1} and I_{Inv2} for an exemplary measured operating point. The total dc-link current I_{Inv} results from the addition of these two currents. In contrast to the dc-current supply from Fig. 1, the battery simulator used here corresponds approximately to a voltage source. However, it should be noted that in the following, the considered signal is not the capacitor current I_C, but the ac-component of the dc-link current. This current is independent of the dc-supply and its impedance. The rms value $I_{\mathrm{Inv,\ AC,RMS}}$ of the operating point shown in Fig. 10 can be looked up in Fig. 11(a) (circled in red). Based on this process, the entire operating area of the electrical motor has been measured. For each operating point, different switching cycle shifts have been set. The resulting $I_{\mathrm{Inv,\ AC,RMS}}$ can be taken from Fig. 11(a). For each of the measured operating points, the operating parameters have been extracted. Based on the extracted operating point parameters, the rms value has been simulated using the MATLAB model already mentioned and calculated analytically in accordance to (41). The values determined by simulation are illustrated in Fig. 11(b). The parameters determined by (41) are depicted in Fig. 11(c). From the comparison of Fig. 11(a) and 11(b), a high correlation can be observed over all analyzed torques, speeds, and σ. On the one hand, this confirms the validity of the underlying measurement setup and the measurement technology used. Furthermore, the applied model and the simulation premises taken into account can be considered suitable. Thus, the reliability of the simulation results support the results already presented in Fig. 6 and confirm the correctness of the prefactor $e^{j(g\sigma - h\beta)}$ examined in Section V. When comparing Fig. 11(a) and (c), the analytically calculated rms values show a reduced characteristic. A clear reduction in the rms values when using a switching cycle shift of $\sigma = \pi/2$ can be

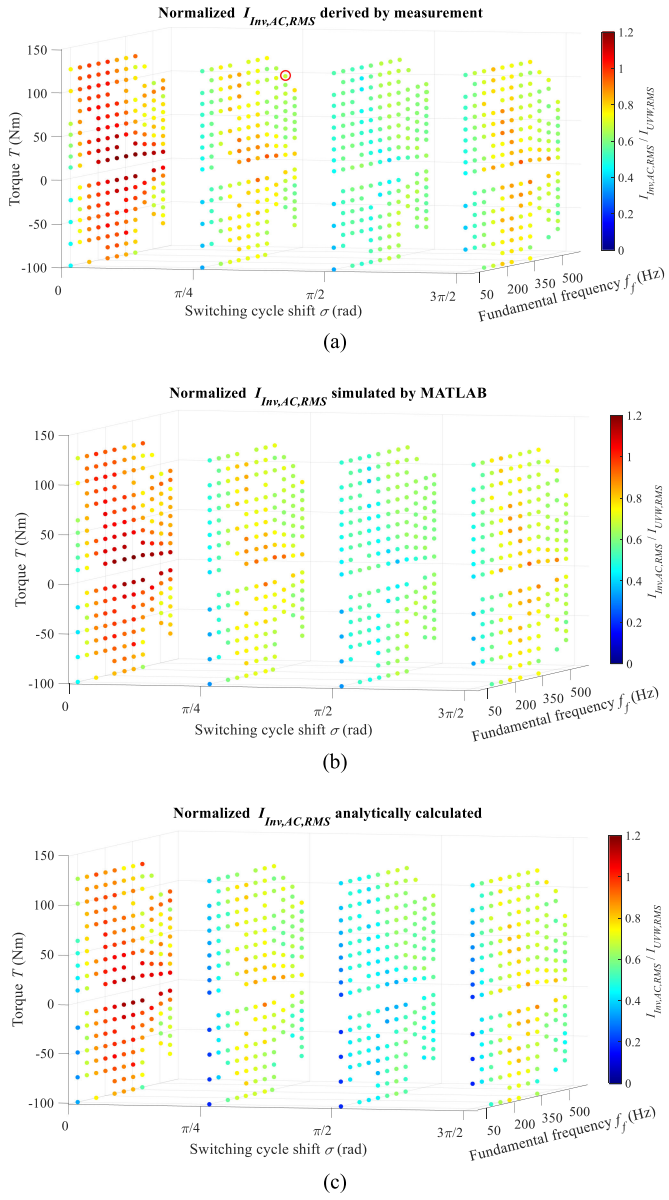

Fig. 11. Comparison of measured, simulated and calculated normalized current $I_{\mathrm{Inv,AC,\,RMS}}$. (a) Derived by measurement. (b) Simulated by MATLAB. (c) Calculated using (41).

seen in both graphics. With an average deviation of 4.8 % from the measured values referenced to $I_{\mathrm{UVW,RMS}}$, the analytical description presented in (41) shows good accuracy. Additionally, the accuracy of the calculated rms value $I_{\mathrm{Inv,AC,RMS}}$ is examined by analogy with the method from Fig. 7(b) for the same operating points. The determined probability of occurrence of a calculated result, normalized on $I_{\mathrm{UVW,RMS}}$, with an error of $<1\%$ is around 36%. An analytically calculated result with an error of $<4\%$ can be achieved with a probability of occurrence of around 87%.

VII. Conclusion

The results presented in this article offer an analytical description of the frequency spectrum of the dc-link current for both the single- and the dual-inverter. This is available in solved form. The use of integral expressions is not necessary. Therefore, the numerical point-by-point integration becomes obsolete. The harmonic amplitudes determined by the Newton–Cotes method show a high correlation with the values determined by simulation. The description of the dual-inverter has been achieved by shifting the phase plot of the description of the single-inverter. This procedure creates the basis for deriving the dc-link current of a multiphase inverter, consisting of n parallel, three-phase two-level inverters. In addition to the analytical description of the harmonics, a definition of the rms value is also presented. This is based on Parseval's theorem. The description of the rms value presented in (41) can be understood as the counterpart of the dual-inverter to the equation of the single-inverter [5, 6]. It defines $I_{\mathrm{Inv,AC,RMS}}$ as a function of σ. The representation of this dependency lays the foundation for a real-time capable optimization of the switching cycle shift of the dual-inverter. A reduction of $I_{\mathrm{Inv,AC,RMS}}$ by more than 40 % for the straight-ahead driving of a vehicle by using an operating point-dependent switching cycle shift has already been proven in [11]. Due to (41), a high-performance optimization option for the entire operating area is now available. The results introduced in this article are presented against the background of the vehicle application. However, the results are valid for all conceivable applications from industry, railway, energy conversion, aerospace, or other areas that contain a dual-inverter. A recommended continuation is the application of the presented methodology to other modulation methods, such as flat-top modulation. This would also favor studies on the operation of a dual or multiphase inverter with different modulation methods. Furthermore, the consideration of current compensation effects in case of parallel stand-alone inverters would be an useful continuation of the discussed topic.

Appendix

If (26) is solved with the methodology explained in Section III-B, the definition (A1), shown on the next page, can be derived.

In analogy with (A1), the definition for the spectrum of the switch current of phase V can be deduced as illustrated in (A2) shown on the next page.

In analogy with (A1), the definition for the spectrum of the switch current of phase W can be deduced as illustrated in (A3) shown at the top of next to next page.

If (30) is solved with the methodology explained in Section III-B, the definition (A4), shown at the top of the next to next page, can be derived.

$$
\begin{aligned}
I_U^{\sim}(f) = \hat{I}_{UVW} \cdot \frac{1}{2\pi} \cdot \Bigg(& \frac{1}{8} \cdot \left(-\cos(-\varphi) \cdot e^{jm\cdot\left(\frac{3}{2}\pi+\frac{3\pi}{8}\cdot M_1\right)} \cdot \frac{j}{m} + \cos(-\varphi) \cdot e^{jm\cdot\left(\frac{\pi}{2}-\frac{3\pi}{8}\cdot M_1\right)} \cdot \frac{j}{m} \right) \\
& + \frac{3}{8} \left(-\cos\left(\frac{\pi}{9}-\varphi\right) \cdot e^{jn\cdot\frac{\pi}{9}+jm\cdot\frac{3\pi}{2}-jm\cdot\frac{\sqrt{3}\pi}{4}\cdot M_1\cdot\sin\left(\frac{13\pi}{9}\right)} \cdot \frac{j}{m} + \cos\left(\frac{\pi}{9}-\varphi\right) \cdot e^{jn\cdot\frac{\pi}{9}+jm\cdot\frac{\pi}{2}+jm\cdot\frac{\sqrt{3}\pi}{4}\cdot M_1\cdot\sin\left(\frac{13\pi}{9}\right)} \cdot \frac{j}{m} \right) \\
& + \frac{3}{8} \left(-\cos\left(\frac{2\pi}{9}-\varphi\right) \cdot e^{jn\cdot\frac{2\pi}{9}+jm\cdot\frac{3\pi}{2}-jm\cdot\frac{\sqrt{3}\pi}{4}\cdot M_1\cdot\sin\left(\frac{14\pi}{9}\right)} \cdot \frac{j}{m} - \cos\left(\frac{2\pi}{9}-\varphi\right) \cdot e^{jn\cdot\frac{2\pi}{9}+jm\cdot\frac{3\pi}{2}-jm\cdot\frac{\sqrt{3}\pi}{4}\cdot M_1\cdot\sin\left(\frac{14\pi}{9}\right)} \cdot \frac{j}{m} \right) \\
& + \frac{1}{8} \left(-\cos\left(\frac{\pi}{3}-\varphi\right) \cdot e^{jn\cdot\frac{\pi}{3}+jm\cdot\left(\frac{3}{2}\pi+\frac{3\pi}{8}\cdot M_1\right)} \cdot \frac{j}{m} + \cos\left(\frac{\pi}{3}-\varphi\right) \cdot e^{jn\cdot\frac{\pi}{3}+jm\cdot\left(\frac{\pi}{2}-\frac{3\pi}{8}\cdot M_1\right)} \cdot \frac{j}{m} \right) \\
& + \frac{1}{8} \left(-\cos\left(\frac{\pi}{3}-\varphi\right) \cdot e^{jn\frac{\pi}{3}+jm\cdot\left(\frac{3}{2}\pi-\frac{3\pi}{8}\cdot M_1+\frac{3\pi}{4}\cdot M_1\right)} \cdot \frac{j}{m} + \cos\left(\frac{\pi}{3}-\varphi\right) \cdot e^{jn\frac{\pi}{3}+jm\cdot\left(\frac{\pi}{2}+\frac{3\pi}{8}\cdot M_1-\frac{3\pi}{4}\cdot M_1\right)} \cdot \frac{j}{m} \right) \\
& + \frac{3}{8} \left(-\cos\left(\frac{4\pi}{9}-\varphi\right) \cdot e^{jn\cdot\frac{4\pi}{9}+jm\cdot\frac{3\pi}{2}+jm\cdot\frac{\sqrt{3}\pi}{4}\cdot M_1\cdot\sin\left(\frac{13\pi}{9}\right)+jm\cdot\frac{\sqrt{3}\pi}{2}M_1\sin\left(\frac{7\pi}{9}\right)} \cdot \frac{j}{m} - \cos\left(\frac{4\pi}{9}-\varphi\right) \right. \\
& \left. \cdot e^{jn\cdot\frac{4\pi}{9}+jm\cdot\frac{3\pi}{2}+jm\cdot\frac{\sqrt{3}\pi}{4}\cdot M_1\cdot\sin\left(\frac{13\pi}{9}\right)+jm\cdot\frac{\sqrt{3}\pi}{2}M_1\sin\left(\frac{7\pi}{9}\right)} \cdot \frac{j}{m} \right) \\
& + \frac{3}{8} \left(-\cos\left(\frac{5\pi}{9}-\varphi\right) \cdot e^{jn\cdot\frac{5\pi}{9}+jm\cdot\frac{3\pi}{2}+jm\cdot\frac{\sqrt{3}\pi}{4}\cdot M_1\cdot\sin\left(\frac{14\pi}{9}\right)+jm\cdot\frac{\sqrt{3}\pi}{2}M_1\sin\left(\frac{8\pi}{9}\right)} \cdot \frac{j}{m} + \cos\left(\frac{5\pi}{9}-\varphi\right) \right. \\
& \left. \cdot e^{jn\cdot\frac{5\pi}{9}+jm\cdot\frac{\pi}{2}-jm\cdot\frac{\sqrt{3}\pi}{4}\cdot M_1\cdot\sin\left(\frac{14\pi}{9}\right)-jm\frac{\sqrt{3}\pi}{2}M_1\cdot\sin\left(\frac{8\pi}{9}\right)} \cdot \frac{j}{m} \right) \\
& + \frac{1}{8} \left(-\cos\left(\frac{2\pi}{3}-\varphi\right) \cdot e^{jn\cdot\frac{2\pi}{3}+jm\cdot\left(\frac{3}{2}\pi-\frac{3\pi}{8}\cdot M_1\right)} \cdot \frac{j}{m} + \cos\left(\frac{2\pi}{3}-\varphi\right) \cdot e^{jn\cdot\frac{2\pi}{3}+jm\cdot\left(\frac{\pi}{2}+\frac{3\pi}{8}\cdot M_1\right)} \cdot \frac{j}{m} \right) \Bigg)
\end{aligned} \tag{A1}
$$

$$
\begin{aligned}
I_V^{\sim}(f) = \hat{I}_{UVW} \cdot \frac{1}{2\pi} \cdot \Bigg(& \frac{1}{8} \cdot \left(-\cos\left(-\varphi-\frac{2\pi}{3}\right) \cdot e^{jm\cdot\left(\frac{3}{2}\pi-\frac{3\pi}{8}\cdot M_1\right)} \cdot \frac{j}{m} + \cos\left(-\varphi-\frac{2\pi}{3}\right) \cdot e^{jm\cdot\left(\frac{\pi}{2}+\frac{3\pi}{8}\cdot M_1\right)} \cdot \frac{j}{m} \right) \\
& + \frac{3}{8} \left(-\cos\left(-\varphi-\frac{5\pi}{9}\right) \cdot e^{jn\cdot\frac{\pi}{9}+jm\cdot\frac{3\pi}{2}+jm\cdot\frac{\sqrt{3}\pi}{4}\cdot M_1\cdot\sin\left(\frac{13\pi}{9}\right)+jm\cdot\frac{\sqrt{3}\pi}{2}\cdot M_1\cdot\sin\left(\frac{\pi}{9}\right)} \cdot \frac{j}{m} + \cos\left(-\varphi-\frac{5\pi}{9}\right) \right. \\
& \left. \cdot e^{jn\cdot\frac{\pi}{9}+jm\cdot\frac{\pi}{2}-jm\cdot\frac{\sqrt{3}\pi}{4}\cdot M_1\cdot\sin\left(\frac{13\pi}{9}\right)-jm\cdot\frac{\sqrt{3}\pi}{2}\cdot M_1\cdot\sin\left(\frac{\pi}{9}\right)} \cdot \frac{j}{m} \right) \\
& + \frac{3}{8} \left(-\cos\left(-\varphi-\frac{4\pi}{9}\right) \cdot e^{jn\cdot\frac{2\pi}{9}+jm\cdot\frac{3\pi}{2}+jm\cdot\frac{\sqrt{3}\pi}{4}\cdot M_1\cdot\sin\left(\frac{14\pi}{9}\right)+jm\cdot\frac{\sqrt{3}\pi}{2}\cdot M_1\cdot\sin\left(\frac{2\pi}{9}\right)} \cdot \frac{j}{m} + \cos\left(-\varphi-\frac{4\pi}{9}\right) \right. \\
& \left. \cdot e^{jn\cdot\frac{2\pi}{9}+jm\cdot\frac{\pi}{2}-jm\cdot\frac{\sqrt{3}\pi}{4}\cdot M_1\cdot\sin\left(\frac{14\pi}{9}\right)-jm\cdot\frac{\sqrt{3}\pi}{2}\cdot M_1\cdot\sin\left(\frac{2\pi}{9}\right)} \cdot \frac{j}{m} \right) \\
& + \frac{1}{8} \left(-\cos\left(-\varphi-\frac{\pi}{3}\right) \cdot e^{jn\cdot\frac{\pi}{3}+jm\cdot\left(\frac{3}{2}\pi+\frac{\sqrt{3}\pi}{4}\cdot M_1\cdot\sin\left(\frac{15\pi}{9}\right)+\frac{\sqrt{3}\pi}{2}\cdot M_1\cdot\sin\left(\frac{\pi}{3}\right)\right)} \cdot \frac{j}{m} + \cos\left(-\varphi-\frac{\pi}{3}\right) \right. \\
& \left. \cdot e^{jn\cdot\frac{\pi}{3}+jm\cdot\left(\frac{\pi}{2}-\frac{\sqrt{3}\pi}{4}\cdot M_1\cdot\sin\left(\frac{15\pi}{9}\right)-\frac{\sqrt{3}\pi}{2}\cdot M_1\cdot\sin\left(\frac{\pi}{3}\right)\right)} \cdot \frac{j}{m} \right) \\
& + \frac{1}{8} \left(-\cos\left(-\varphi-\frac{\pi}{3}\right) \cdot e^{jn\frac{\pi}{3}+jm\cdot\left(\frac{3}{2}\pi-\frac{\sqrt{3}\pi}{4}\cdot M_1\cdot\sin\left(\frac{4\pi}{3}\right)\right)} \cdot \frac{j}{m} + \cos\left(-\varphi-\frac{\pi}{3}\right) \cdot e^{jn\frac{\pi}{3}+jm\cdot\left(\frac{\pi}{2}+\frac{\sqrt{3}\pi}{4}\cdot M_1\cdot\sin\left(\frac{4\pi}{3}\right)\right)} \cdot \frac{j}{m} \right) \\
& + \frac{3}{8} \left(-cos\left(-\varphi-\frac{2\pi}{9}\right) \cdot e^{jn\cdot\frac{4\pi}{9}+jm\cdot\frac{3\pi}{2}-jm\cdot\frac{\sqrt{3}\pi}{4}\cdot M_1\cdot\sin\left(\frac{13\pi}{9}\right)} \cdot \frac{j}{m} + cos\left(-\varphi-\frac{2\pi}{9}\right) \cdot e^{jn\cdot\frac{4\pi}{9}+jm\cdot\frac{\pi}{2}+jm\cdot\frac{\sqrt{3}\pi}{4}\cdot M_1\cdot\sin\left(\frac{13\pi}{9}\right)} \cdot \frac{j}{m} \right) \\
& + \frac{3}{8} \left(-cos\left(-\varphi-\frac{\pi}{9}\right) \cdot e^{jn\cdot\frac{5\pi}{9}+jm\cdot\frac{3\pi}{2}-jm\cdot\frac{\sqrt{3}\pi}{4}\cdot M_1\cdot\sin\left(\frac{14\pi}{9}\right)} \cdot \frac{j}{m} + cos\left(-\varphi-\frac{\pi}{9}\right) \cdot e^{jn\cdot\frac{5\pi}{9}+jm\cdot\frac{\pi}{2}+jm\cdot\frac{\sqrt{3}\pi}{4}\cdot M_1\cdot\sin\left(\frac{14\pi}{9}\right)} \cdot \frac{j}{m} \right) \\
& + \frac{1}{8} \left(-\cos(-\varphi) \cdot e^{jn\cdot\frac{2\pi}{3}+jm\cdot\left(\frac{3}{2}\pi-\frac{\sqrt{3}\pi}{4}\cdot M_1\cdot\sin\left(\frac{5\pi}{3}\right)\right)} \cdot \frac{j}{m} + \cos(-\varphi) \cdot e^{jn\cdot\frac{2\pi}{3}+jm\cdot\left(\frac{\pi}{2}+\frac{\sqrt{3}\pi}{4}\cdot M_1\cdot\left(\frac{5\pi}{3}\right)\right)} \cdot \frac{j}{m} \right) \Bigg)
\end{aligned} \tag{A2}
$$

$$
\begin{aligned}
I_{\widetilde{W}}\ (f) = \hat{I}_{UVW}\ \cdot \tfrac{1}{2\pi} \cdot \Bigg(& \tfrac{1}{8} \cdot \Bigg(-\cos\left(\tfrac{2\pi}{3} - \varphi\right) \cdot e^{jm \cdot \left(\frac{3}{2}\pi + \frac{\sqrt{3}\pi}{4} \cdot M_1 \cdot \sin\left(\frac{4\pi}{3}\right)\right)} \cdot \tfrac{j}{m} + \cos\left(\tfrac{2\pi}{3} - \varphi\right) \cdot e^{jm \cdot \left(\frac{\pi}{2} - \frac{\sqrt{3}\pi}{4} \cdot M_1 \cdot \sin\left(\frac{4\pi}{3}\right)\right)} \cdot \tfrac{j}{m} \Bigg) \\
& + \tfrac{3}{8} \Bigg(-\cos\left(\tfrac{7\pi}{9} - \varphi\right) \cdot e^{jn \cdot \frac{\pi}{9} + jm \cdot \left(\frac{3\pi}{2} + \frac{\sqrt{3}\pi}{4} \cdot M_1 \cdot \sin\left(\frac{13\pi}{9}\right)\right)} \cdot \tfrac{j}{m} + \cos\left(\tfrac{7\pi}{9} - \varphi\right) \cdot e^{jn \cdot \frac{\pi}{9} + jm \cdot \left(\frac{\pi}{2} - \frac{\sqrt{3}\pi}{4} \cdot M_1 \cdot \sin\left(\frac{13\pi}{9}\right)\right)} \cdot \tfrac{j}{m} \Bigg) \\
& + \tfrac{3}{8} \Bigg(-\cos\left(\tfrac{8\pi}{9} - \varphi\right) \cdot e^{jn \cdot \frac{2\pi}{3} + jm \cdot \left(\frac{3\pi}{2} + \frac{\sqrt{3}\pi}{4} \cdot M_1 \cdot \sin\left(\frac{14\pi}{9}\right)\right)} \cdot \tfrac{j}{m} + \cos\left(\tfrac{8\pi}{9} - \varphi\right) \cdot e^{jn \cdot \frac{2\pi}{9} + jm \cdot \left(\frac{\pi}{2} - \frac{\sqrt{3}\pi}{4} \cdot M_1 \cdot \sin\left(\frac{14\pi}{9}\right)\right)} \cdot \tfrac{j}{m} \Bigg) \\
& + \tfrac{1}{8} \Bigg(-\cos\left(\pi - \varphi\right) \cdot e^{jn \cdot \frac{\pi}{3} + jm \cdot \left(\frac{3}{2}\pi + \frac{\sqrt{3}\pi}{4} \cdot M_1 \cdot \sin\left(\frac{5\pi}{3}\right)\right)} \cdot \tfrac{j}{m} + \cos\left(\pi - \varphi\right) \cdot e^{jn \cdot \frac{\pi}{3} + jm \cdot \left(\frac{\pi}{2} - \frac{\sqrt{3}\pi}{4} \cdot M_1 \cdot \sin\left(\frac{5\pi}{3}\right)\right)} \cdot \tfrac{j}{m} \Bigg) \\
& + \tfrac{1}{8} \Bigg(-\cos\left(\pi - \varphi\right) \cdot e^{jn \frac{\pi}{3} + jm \cdot \left(\frac{3}{2}\pi + \frac{\sqrt{3}\pi}{4} \cdot M_1 \cdot \sin\left(\frac{4\pi}{3}\right)\right)} \cdot \tfrac{j}{m} + \cos\left(\pi - \varphi\right) \cdot e^{jn \frac{\pi}{3} + jm \cdot \left(\frac{\pi}{2} - \frac{\sqrt{3}\pi}{4} \cdot M_1 \cdot \sin\left(\frac{4\pi}{3}\right)\right)} \cdot \tfrac{j}{m} \Bigg) \\
& + \tfrac{3}{8} \Bigg(-\cos\left(\tfrac{10\pi}{9} - \varphi\right) \cdot e^{jn \cdot \frac{4\pi}{9} + jm \cdot \left(\frac{3\pi}{2} + \frac{\sqrt{3}\pi}{4} \cdot M_1 \cdot \sin\left(\frac{13\pi}{9}\right)\right)} \cdot \tfrac{j}{m} + \cos\left(\tfrac{10\pi}{9} - \varphi\right) \cdot e^{jn \cdot \frac{4\pi}{9} + jm \cdot \left(\frac{\pi}{2} - \frac{\sqrt{3}\pi}{4} \cdot M_1 \cdot \sin\left(\frac{13\pi}{9}\right)\right)} \cdot \tfrac{j}{m} \Bigg) \\
& + \tfrac{3}{8} \Bigg(-\cos\left(\tfrac{11\pi}{9} - \varphi\right) \cdot e^{jn \cdot \frac{5\pi}{9} + jm \cdot \left(\frac{3\pi}{2} + \frac{\sqrt{3}\pi}{4} \cdot M_1 \cdot \sin\left(\frac{14\pi}{9}\right)\right)} \cdot \tfrac{j}{m} + \cos\left(\tfrac{11\pi}{9} - \varphi\right) \cdot e^{jn \cdot \frac{5\pi}{9} + jm \cdot \left(\frac{\pi}{2} - \frac{\sqrt{3}\pi}{4} \cdot M_1 \cdot \sin\left(\frac{14\pi}{9}\right)\right)} \cdot \tfrac{j}{m} \Bigg) \\
& + \tfrac{1}{8} \Bigg(-\cos\left(\tfrac{12\pi}{9} - \varphi\right) \cdot e^{jn \cdot \frac{6\pi}{9} + jm \cdot \left(\frac{3}{2}\pi + \frac{\sqrt{3}\pi}{4} \cdot M_1 \cdot \sin\left(\frac{15\pi}{9}\right)\right)} \cdot \tfrac{j}{m} + \cos\left(\tfrac{12\pi}{9} - \varphi\right) \cdot e^{jn \cdot \frac{6\pi}{3} + jm \cdot \left(\frac{\pi}{2} - \frac{\sqrt{3}\pi}{4} \cdot M_1 \cdot \left(\frac{15\pi}{9}\right)\right)} \cdot \tfrac{j}{m} \Bigg) \Bigg)
\end{aligned}
\tag{A3}
$$

$$
\begin{aligned}
I_{\widetilde{R}}\ (f) = \hat{I}_{\mathrm{RST}}\ \cdot \frac{1}{2\pi} \cdot e^{j(g \cdot \sigma - h \cdot \beta)} & \left(\frac{1}{8} \cdot \left(-\cos\left(-\varphi\right) \cdot e^{jg \cdot \left(\frac{3}{2}\pi + \frac{3\pi}{8} \cdot M_2\right)} \cdot \frac{j}{g} + \cos\left(-\varphi\right) \cdot e^{jg \cdot \left(\frac{\pi}{2} - \frac{3\pi}{8} \cdot M_2\right)} \cdot \frac{j}{g} \right) \right. \\
& + \frac{3}{8} \left(-\cos\left(\frac{\pi}{9} - \varphi\right) \cdot e^{jh \cdot \frac{\pi}{9} + jg \cdot \frac{3\pi}{2} - jg \cdot \frac{\sqrt{3}\pi}{4} \cdot M_2 \cdot \sin\left(\frac{13\pi}{9}\right)} \cdot \frac{j}{g} + \cos\left(\frac{\pi}{9} - \varphi\right) \cdot e^{jh \cdot \frac{\pi}{9} + jg \cdot \frac{\pi}{2} + jg \cdot \frac{\sqrt{3}\pi}{4} \cdot M_2 \cdot \sin\left(\frac{13\pi}{9}\right)} \cdot \frac{j}{g} \right) \\
& + \frac{3}{8} \left(-\cos\left(\frac{2\pi}{9} - \varphi\right) \cdot e^{jh \cdot \frac{2\pi}{9} + jg \cdot \frac{3\pi}{2} - jg \cdot \frac{\sqrt{3}\pi}{4} \cdot M_2 \cdot \sin\left(\frac{14\pi}{9}\right)} \cdot \frac{j}{g} + \cos\left(\frac{2\pi}{9} - \varphi\right) \cdot e^{jh \cdot \frac{2\pi}{9} + jg \cdot \frac{\pi}{2} + jg \cdot \frac{\sqrt{3}\pi}{4} \cdot M_2 \cdot \sin\left(\frac{14\pi}{9}\right)} \cdot \frac{j}{g} \right) \\
& + \frac{1}{8} \left(-\cos\left(\frac{\pi}{3} - \varphi\right) \cdot e^{jh \cdot \frac{\pi}{3} + jg \cdot \left(\frac{3}{2}\pi + \frac{3\pi}{8} \cdot M_2\right)} \cdot \frac{j}{g} + \cos\left(\frac{\pi}{3} - \varphi\right) \cdot e^{jh \cdot \frac{\pi}{3} + jg \cdot \left(\frac{\pi}{2} - \frac{3\pi}{8} \cdot M_2\right)} \cdot \frac{j}{g} \right) \\
& + \frac{1}{8} \left(-\cos\left(\frac{\pi}{3} - \varphi\right) \cdot e^{jh \frac{\pi}{3} + jg \cdot \left(\frac{3}{2}\pi - \frac{3\pi}{8} \cdot M_2 + \frac{3\pi}{4} \cdot M_2\right)} \cdot \frac{j}{g} + \cos\left(\frac{\pi}{3} - \varphi\right) \cdot e^{jh \frac{\pi}{3} + jg \cdot \left(\frac{\pi}{2} + \frac{3\pi}{8} \cdot M_2 - \frac{3\pi}{4} \cdot M_2\right)} \cdot \frac{j}{g} \right) \\
& + \frac{3}{8} \left(-cos\ \left(\frac{4\pi}{9} - \varphi\right) \cdot e^{jh \cdot \frac{4\pi}{9} + jg \cdot \frac{3\pi}{2} + jg \cdot \frac{\sqrt{3}\pi}{4} \cdot M_2 \cdot \sin\left(\frac{13\pi}{9}\right) + jg \cdot \frac{\sqrt{3}\pi}{2} M_2 \sin\left(\frac{7\pi}{9}\right)} \cdot \frac{j}{g} + \cos\left(\frac{4\pi}{9} - \varphi\right) \right. \\
& \left. \cdot e^{jh \cdot \frac{4\pi}{9} + jg \cdot \frac{\pi}{2} - jg \cdot \frac{\sqrt{3}\pi}{4} \cdot M_2 \cdot \sin\left(\frac{13\pi}{9}\right) - jg \frac{\sqrt{3}\pi}{2} M_2 \cdot \sin\left(\frac{7\pi}{9}\right)} \cdot \frac{j}{g} \right) \\
& + \frac{3}{8} \left(-cos\left(\frac{5\pi}{9} - \varphi\right) \cdot e^{jh \cdot \frac{5\pi}{9} + jg \cdot \frac{3\pi}{2} + jg \cdot \frac{\sqrt{3}\pi}{4} \cdot M_2 \cdot \sin\left(\frac{14\pi}{9}\right) + jg \cdot \frac{\sqrt{3}\pi}{2} M_2 \sin\left(\frac{8\pi}{9}\right)} \cdot \frac{j}{g} + \cos\left(\frac{5\pi}{9} - \varphi\right) \right. \\
& \left. \cdot e^{jh \cdot \frac{5\pi}{9} + jg \cdot \frac{\pi}{2} - jg \cdot \frac{\sqrt{3}\pi}{4} \cdot M_2 \cdot \sin\left(\frac{14\pi}{9}\right) - jg \frac{\sqrt{3}\pi}{2} M_2 \cdot \sin\left(\frac{8\pi}{9}\right)} \cdot \frac{j}{g} \right) \\
& \left. + \frac{1}{8} \left(-\cos\left(\frac{2\pi}{3} - \varphi\right) \cdot e^{jh \cdot \frac{2\pi}{3} + jg \cdot \left(\frac{3}{2}\pi - \frac{3\pi}{8} \cdot M_2\right)} \cdot \frac{j}{g} + \cos\left(\frac{2\pi}{3} - \varphi\right) \cdot e^{jh \cdot \frac{2\pi}{3} + jg \cdot \left(\frac{\pi}{2} + \frac{3\pi}{8} \cdot M_2\right)} \cdot \frac{j}{g} \right) \right)
\end{aligned}
\tag{A4}
$$

REFERENCES

[1] M. Schiedermeier, C. Rettner, M. Heilmann, F. Schneider, and M. März, "Interference of automotive HV-DC-systems by traction voltage-source-inverters (VSI)," in *Proc. IEEE Transp. Electrific. Conf.*, 2019, doi: 10.1109/ITEC-India48457.2019.ITECINDIA2019-37.

[2] A. Emadi, A. Khaligh, C. H. Rivetta, and G. A. Williamson, "Constant power loads and negative impedance instability in automotive systems: definition, modeling, stability, and control of power electronic converters and motor drives," *IEEE Trans. Veh. Technol.*, vol. 55, no. 4, pp. 1112–1125, Jul. 2006, doi: 10.1109/TVT.2006.877483.

[3] H. Ye and A. Emadi, "A six-phase current reconstruction scheme for dual traction inverters in hybrid electric vehicles with a single DC-link current sensor," *IEEE Trans. Veh. Technol.*, vol. 63, no. 7, pp. 3085–3093, Sep. 2014, doi: 10.1109/TVT.2014.2305637.

[4] H. Ye and A. Emadi, "An interleaving scheme to reduce DC-link current harmonics of dual traction inverters in hybrid electric vehicles," in *Proc. IEEE Appl . Power Electron. Conf. Expo.*, 2014, pp. 3205–3211, doi: 10.1109/2014.6803764.APEC.

[5] F. Renken, "Analytic calculation of the DC-link capacitor current for pulsed three-phase inverters," in *Proc. 11th Int. Conf. Power Electron. Motion Control*, 2004.

[6] J. W. Kolar and S. D. Round, "Analytical calculation of the RMS current stress on the DC-link capacitor of voltage-PWM converter systems," *IEEE Proc. Electr. Power Appl.*, vol. 4, 2006, Art. no. 535, doi: 10.1049/ip-epa:20050458.
[7] M. H. Bierhoff and F. W. Fuchs, "DC-Link harmonics of three-phase voltage-source converters influenced by the pulsewidth-modulation strategy—an analysis," *IEEE Trans. Ind. Electron.*, vol. 55, no. 5, pp. 2085–2092, May 2008, doi: 10.1109/TIE.2008.921203.
[8] A. Voldoire, J.-L. Schanen, J.-P. Ferrieux, C. Gautier, and C. Saber, "Analytical calculation of DC-link current for N-interleaved 3-phase PWM inverters considering AC current ripple," in *Proc. 21st Eur. Conf. Power Electron. Appl.*, 2019, doi: 10.23919/EPE.2019.8915183.
[9] G.-J. Su and L. Tang, "A segmented traction drive system with a small dc bus capacitor," in *Proc. IEEE Energy Convers. Congr.*, 2012, pp. 2847–2853, doi: 10.1109/ECCE.2012.6342375.
[10] Q. Cen, W. Xie, and Y. Lu, "Research on optimizing control of high-power dual-inverter drive system," in *Proc. IEEE Int. Symp. Ind. Electron.*, 2012, pp. 486–489, doi: 10.1109/ISIE.2012.6237135.
[11] M. Schiedermeier, C. Rettner, M. Steiner, and M. März, "Dual-inverter control synchronization strategy to minimize the DC-link capacitor current," in *Proc. IEEE Veh. Power Propulsion Conf.*, 2020.
[12] X. Lyu, H. Zhou, B. Curuvija, and D. Cao, "DC-link RMS current reduction by increasing paralleled 3-phase inverter module number for segmented traction drive," in *Proc. IEEE Appl. Power Electron. Conf. Expo.*, 2017, pp. 906–911, doi: 10.1109/.2017.7930804APEC.
[13] L. Jin and J. Zhang, "Modeling of DC link capacitor current ripple for electric vehicle traction converter," OTREC-SS-634, Portland, OR: Transportation Research and Education Center (TREC), 2010, [online]. Available: https://doi.org/10.15760/trec.40.
[14] C. Rettner, G. Jacob, M. Schiedermeier, A. Apelsmeier, and M. März, "Voltage ripple analysis based on DC-link current harmonics for voltage Source Inverters," in *Proc. 20th Workshop Control Model. Power Electron.*, 2019, doi: 10.1109/COMPEL.2019.8769623.
[15] G. Holmes and T. A. Lipo, "*Pulse Width Modulation for Power Converters: Principles and Practice*. 2003.
[16] G. Bärwolf, Numerik für Ingenieure, *Physiker und Informatiker*. München: Spektrum, 2007.
[17] R. W. Freund and R. H. W. Hoppe, *Numerische Mathematik 1. 10. Auflage*. Berlin, Germany: Springer, 2007.
[18] M. R. Schäferkotter and P. K. Kythe, *Handbook of Computational Methods for Integration*. Boca Raton, FL, USA: Chapman & Hall, 2005.
[19] H. R. Schwarz and N. Köckler, *Numerische Mathematik. 6. Auflage. Teubner, Stuttgart*. Stuttgart, Germany: Teubner, 2006.
[20] D. Roddy, "A method of using Simpson's rule in the DFT," *IEEE Trans. Acoust., Speech, Signal Process.*, vol. 29, no. 4, pp. 936–937, Aug. 1981, doi: 10.1109/TASSP.1981.1163629.
[21] B. R. Hunt, "Spectral effects in the use of newton—cotes approximations for computing discrete fourier transforms," *IEEE Trans. Comput.*, vol. C-20, no. 8, pp. 942–943, Aug. 1971, doi: 10.1109/T-C.1971.223378.
[22] L. Papula, *Mathematik für Ingenieure und Naturwissenschaftler (Band 2)*, Wiesbaden, Germany: Vieweg+Teubner, 2009.

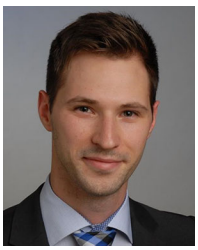

Maximilian Schiedermeier was born in Ingolstadt, Germany, in 1988. He received the Dipl.-Ing. (FH) degree in electrical engineering, electronics and information technology from the University of Applied Sciences Ingolstadt, Ingolstadt, Germany in 2012. He is currently working toward the Ph.D. degree in electrical engineering with the Chair of Power Electronics, University of Erlangen-Nuremberg (FAU), Germany.

Since 2015, he has been with AUDI AG, Ingolstadt, Germany, as a Research and Development Engineer. His fields of interest include voltage-source-inverters for automotive applications and the reduction of their dc-link noise.

Franziska Schlamp received the B.Sc. and M.Sc. degrees in mathematics from the Catholic University of Eichstaett-Ingolstadt, Germany in 2017 and 2020, respectively.

Her research interests include the mathematical background of electro mobility.

Cornelius Rettner received the B.Sc. and the M.Sc. degrees in electrical engineering, electronics, and information technology from the University of Erlangen-Nuremberg (FAU), Germany, in 2014 and 2016, respectively. He is currently working toward the Ph.D. degree in electrical engineering with the Chair of Power Electronics, University of Erlangen-Nuremberg and the AUDI AG, Ingolstadt, Germany.

His current research interests include dc-link capacitors of automotive traction inverters and HV-dc-systems of electric vehicles.

Martin März received the Diploma and Ph.D. degrees in electrical engineering from the University of Erlangen-Nuremberg (FAU), Germany, in 1988 and 1995 respectively.

During his Ph.D. with the Institute of Microwaves and Photonics at the FAU, his research focus was on microwave excitation of CO2 lasers. In 1995, he started his professional career in the semiconductor division with Siemens (later Infineon Technologies AG) in Munich, Germany. Since 2000, he has been the Head with the Power Electronics System Department, at the Fraunhofer Institute of Integrated Systems and Device Technology IISB, Erlangen, where he has been the Deputy Director, since 2012, the Acting Director, since 2018. In 2016, he was appointed as a Full Professor to the newly established Chair of Power Electronics at the FAU. His research interests include innovative technologies for power electronics with a focus on very high power density and efficiency, thermal management, system integration, and cognitive power electronics.